Computers & Fluids 95 (2014) 197–209

Contents lists available at ScienceDirect

Computers & Fluids

journal homepage: www.elsevier.com/locate/compfluid

A spectral-element discontinuous Galerkin lattice Boltzmann method for simulating natural convection heat transfer in a horizontal concentric annulus

Saumil Sudhir Patel [a], Misun Min [b], Kalu Chibueze Uga [a], Taehun Lee [a,*]

[a] Department of Mechanical Engineering, City College of City University of New York, New York, NY 10031, USA
[b] Mathematics and Computer Science Division, Argonne National Laboratory, Argonne, IL 60439, USA

ARTICLE INFO

Article history:
Received 15 August 2013
Received in revised form 30 December 2013
Accepted 19 February 2014
Available online 12 March 2014

Keywords:
Thermal lattice Boltzmann method
Spectral-element method
Discontinuous Galerkin method
Natural convection flow

ABSTRACT

We present a spectral-element discontinuous Galerkin lattice Boltzmann method to solve incompressible natural convection flows based on the Bousinessq approximation. A passive-scalar thermal lattice Boltzmann model is used to resolve flows for variable Prandtl number. In our model, we solve the lattice Boltzmann equation for the velocity field and the advection–diffusion equation for the temperature field. As a result, we reduce the degrees of freedom when compared with the passive-scalar double-distribution model, which requires the solution of several equations to resolve the temperature field. Our numerical solution is represented by the tensor product basis of the one-dimensional Legendre–Lagrange interpolation polynomials. A high-order discretization is employed on body-conforming hexahedral elements with Gauss–Lobatto–Legendre quadrature nodes. Within the discontinuous Galerkin framework, we weakly impose boundary and element-interface conditions through the numerical flux. A fourth-order Runge–Kutta scheme is used for time integration with no additional cost for mass matrix inversion due to fully diagonal mass matrices. We study natural convection fluid flows in a square cavity and a horizontal concentric annulus for Rayleigh numbers in the range of $Ra = 10^3$–10^8. We validate our numerical approach by comparing it with finite-difference, finite-volume, multiple-relaxation-time lattice Boltzmann, and spectral-element methods. Our computational results show good agreement in temperature profiles and Nusselt numbers using relatively coarse resolutions.

1. Introduction

Natural convection flow simulations have been an active area of research for many years. These flows are set in motion by a buoyancy force that occurs as a result of a small density gradient and the presence of an external force such as gravity. Understanding the behavior of natural convection flows is important in nuclear reactor design, cooling of electronic equipment, and determination of heat loss from steam pipes.

In recent decades, thermal lattice Boltzmann methods (TLBMs) have emerged as reliable methods for simulating natural convection flows. TLBMs generally fall into two approaches: the multispeed approach and the passive-scalar approach. The multispeed approach is an extension of the isothermal model, where the density distribution function is solely used to describe the mass, momentum, and temperature [1,2]. The passive-scalar approach uses additional equations, independent of the density distribution, to describe the temperature. When viscous heating and compression work due to pressure are negligible, as is the case in most natural convection flows, the temperature does not influence the momentum—it is advected and diffused "passively" [3].

The multispeed approach does have limitations. In particular, it suffers from severe numerical instability and restricts the Prandtl (Pr) number to a fixed quantity [1]. However, numerous models have been proposed to rectify these issues. In [4], McNamara et al. were able to improve the stability by implementing a Lax–Wendroff advection scheme. Using higher-order symmetric velocity lattices, Vahala et al. [5] showed better stability properties over lower-order symmetric lattices. Prasianakis and Karlin [6] built a model using the standard velocity lattice (D2Q9), which incorporated equilibrium expansions up to the fourth order in velocity and correction terms to the lattice Boltzmann equation (LBE) in order to enhance stability for high Rayleigh number (Ra) flow. The correction terms also allowed their model to investigate

* Corresponding author. Tel.: +1 (212) 650 6122.
E-mail addresses: saumil.patel134@gmail.com (S.S. Patel), mmin@mcs.anl.gov (M. Min), uga.kalu@gmail.com (K.C. Uga), thlee@ccny.cuny.edu (T. Lee).

http://dx.doi.org/10.1016/j.compfluid.2014.02.021
0045-7930/

variable *Pr*. Watari and Tsutahara [7] proposed a finite-difference lattice Boltzmann method (FDLBM) that utilized a second-order upwinding difference scheme to improve stability. And to investigate variable *Pr*, Soe et al. [8] introduced an extended collision matrix without affecting the stability.

One version of the passive-scalar approach utilizes a double-distribution model based on the multiple component LBE proposed by Shan and Chen [3]. In this approach, one component (i.e., density distribution function) represents motion of the fluid and the other (i.e., energy distribution function) describes the passive temperature field. Two independent relaxation times are utilized for each component, thus allowing for variable *Pr*. In [9], Shan showed that the double-distribution model enhanced numerical stability over the multispeed approach for high *Ra*. He et al. [10] also proposed a double-distribution model in which the density distribution function recovers the macroscopic mass and momentum variables while an internal energy density distribution function recovers the energy. Because the model in [10] directly solves evolution of the internal energy, a Chapman–Enskog multiscale expansion analysis shows that viscous heat dissipation and compression work are correctly recovered in the macroscopic energy equation.

Since the work of He et al. [10], simpler double-distribution models have been proposed in the incompressible limit. Both Palmer and Rector [11] and Peng et al. [12] neglected viscous dissipation entirely and dropped complicated spatial gradients to study Rayleigh-Bénard convection and natural convection within a square cavity. In [13], Shi et al. proposed a double-distribution model that incorporates only viscous heat dissipation to study thermal Couette flow. Guo et al. [14] proposed a double-distribution model based on the total energy, which allows for a simpler computation of viscous dissipation and compression work. Others have proposed smaller lattice velocity models for the energy distribution functions [15].

The double-distribution model has also been used on irregular or unstructured grids to handle natural convection flows. Dixit and Babu [16] employed an interpolation supplemented lattice Boltzmann method [17] on a nonuniform mesh to study natural convection in a square at $Ra > 10^6$. Shi et al. [18] extended the method proposed by Guo and Zhao [19] and used FDLBM on the polar representation of the double-distribution model. Shu et al. [20] used a Taylor series expansion and least-squares-based lattice Boltzmann method (TLLBM) to solve the double-distribution model. The TLLBM has proved useful for complex geometries [21]. Finite-volume lattice Boltzmann methods (FVLBMs) have also been proposed and implemented on unstructured meshes [22]. Although FVLBM has been applied to isothermal flows, an extension to either a multispeed or double-distribution model seems feasible.

Another passive-scalar approach is to solve the macroscopic energy equation for the temperature and couple it with the isothermal LBE in order to resolve the velocity. This approach is beneficial for flows with negligible viscous dissipation, and therefore the macroscopic energy equation simplifies to an advection–diffusion equation for the temperature. This model eliminates the need to solve multiple equations as is required in the double-distribution model. In addition, flows with variable *Pr* number can be investigated. Lallemand and Luo [23] proposed this type of approach, solving the advection–diffusion equation for the temperature using a finite-difference method. They showed enhanced stability for simple Cartesian geometries such as a cubic box. For complex geometries, however, finite-difference stencils may not have the same symmetries as the underlying discrete velocity, and extrapolation might cause loss of local conservation.

Implementation of physically accurate hydrodynamic and thermal boundary conditions is crucial in both the multispeed and passive-scalar models. Extensive research on boundary treatment techniques has been done and we refer the reader to the following literature: [24–30].

In this paper, we present a spectral-element discontinuous Galerkin (SEDG) method to solve a passive-scalar thermal lattice Boltzmann model. Our numerical scheme is extended from the previously developed spectral-element discontinuous Galerkin lattice Boltzmann method (SEDG-LBM) presented in [31]. We include a force term, resulting from the Bousinessq approximation [9], into the discrete Boltzmann (DB) and lattice Boltzmann (LB) equations. This approach allows us to examine flows in the incompressible limit (i.e. for low Mach (*Ma*) numbers and small density fluctuations).

We use the SEDG-LBM to solve the LBE for the density distribution function thereby resolving the mass and momentum conservation laws. With proper coupling to the LBE, we then determine the temperature field by solving the advection–diffusion (i.e. energy) equation. We use a high-order spectral-element discontinuous Galerkin (SEDG) discretization based on the tensor product basis of the one-dimensional Legendre–Lagrange interpolation polynomials. Our SEDG discretization is employed upon body-conforming hexahedral elements with Gauss–Lobatto–Legendre (GLL) grid points. Bounceback boundary conditions are applied weakly through the numerical flux without the additional effort of interpolation for complex geometries as required by other lattice Boltzmann (LB) schemes [25–27].

The paper is organized as follows. In Section 2, we present the governing equations, namely, the LBE with a Bousinessq approximation and the advection–diffusion equation. In Section 3, we discuss the formulation of our numerical scheme. Section 4 presents computational results and their validation for natural convection heat transfer in a square cavity and horizontal concentric annulus. We discuss our conclusions in Section 5.

2. Governing equations

In this section we describe our governing equations for natural convection flows. We derive the lattice Boltzmann equation with a forcing term and the formulation for the collision and streaming steps. We also present a simplified macroscopic energy equation for incompressible natural convection flows.

2.1. Lattice Boltzmann equation: Collision and Streaming

We write the discrete Boltzmann equation with a forcing term, where the collision term is approximated by the Bhatnagar–Gross–Krook, or single-relaxation-time, operator [32]:

$$\frac{\partial f_\alpha}{\partial t} + \mathbf{e}_\alpha \cdot \nabla f_\alpha = -\frac{f_\alpha - f_\alpha^{eq}}{\lambda} + \frac{(\mathbf{e}_\alpha - \mathbf{u}) \cdot \mathbf{G} f_\alpha^{eq}}{\rho c_s^2}, \tag{1}$$

where f_α $(\alpha = 0, 1, \ldots, N_\alpha)$ is the particle density distribution function defined in the direction of the microscopic velocity $\mathbf{e}_\alpha$, λ is the relaxation time, and N_α is the number of microscopic velocities. We consider the two-dimensional 9-velocity model (D2Q9) associated with $\mathbf{e}_\alpha = (0,0)$ for $\alpha = 0$; $\mathbf{e}_\alpha = (\cos\theta_\alpha, \sin\theta_\alpha)$ with $\theta_\alpha = (\alpha - 1)\pi/2$ for α = 1, 2, 3, 4; and $\mathbf{e}_\alpha = \sqrt{2}(\cos\phi_\alpha, \sin\phi_\alpha)$ with $\phi_\alpha = (\alpha - 5)\pi/2 + \pi/4$ for α = 5, 6, 7, 8. The second term on the right-hand side of Eq. (1) represents the force term. **G** is the external body force, depending on space and time. We consider a Bousinessq approximation for **G**. Details on the formulation for **G** are discussed in Section 4. The equilibrium distribution function is given by

$$f_\alpha^{eq} = t_\alpha \rho \left[1 + \frac{(\mathbf{e}_\alpha \cdot \mathbf{u})}{c_s^2} + \frac{(\mathbf{e}_\alpha \cdot \mathbf{u})^2}{2c_s^4} - \frac{(\mathbf{u} \cdot \mathbf{u})}{2c_s^2} \right], \tag{2}$$

where ρ is the density; $\mathbf{u}$ is the macroscopic velocity; $t_0 = 4/9, t_{\alpha=1,4} = 1/9$, and $t_{\alpha=5,8} = 1/36$ are the weights; and

$c_s = 1/\sqrt{3}$ is the speed of sound [33]. We obtain the LBE by discretizing Eq. (1) along characteristics over the time step δt as shown in [31].

$$f_\alpha(\mathbf{x},t) - f_\alpha(\mathbf{x}-\mathbf{e}_\alpha\delta t, t-\delta t) = -\int_{t-\delta t}^{t} \frac{f_\alpha - f_\alpha^{eq}}{\lambda} dt' + \int_{t-\delta t}^{t} \frac{(\mathbf{e}_\alpha - \mathbf{u})\cdot \mathbf{G} f_\alpha^{eq}}{\rho c_s^2} dt' \tag{3}$$

Applying the trapezoidal rule for the integration on the right-hand side of Eq. (3), we have the following for each term

$$\int_{t-\delta t}^{t} \frac{f_\alpha - f_\alpha^{eq}}{\lambda} dt' \approx \frac{f_\alpha - f_\alpha^{eq}}{2\tau}\bigg|_{(\mathbf{x}-\mathbf{e}_\alpha\delta t, t-\delta t)} + \frac{f_\alpha - f_\alpha^{eq}}{2\tau}\bigg|_{(\mathbf{x},t)} \tag{4}$$

and

$$\int_{t-\delta t}^{t} \frac{(\mathbf{e}_\alpha - \mathbf{u})\cdot \mathbf{G} f_\alpha^{eq}}{\rho c_s^2} dt' \approx \delta t \frac{(\mathbf{e}_\alpha - \mathbf{u})\cdot \mathbf{G} f_\alpha^{eq}}{2\rho c_s^2}\bigg|_{(\mathbf{x}-\mathbf{e}_\alpha\delta t, t-\delta t)} + \delta t \frac{(\mathbf{e}_\alpha - \mathbf{u})\cdot \mathbf{G} f_\alpha^{eq}}{2\rho c_s^2}\bigg|_{(\mathbf{x},t)}, \tag{5}$$

where the dimensionless relaxation time is $\tau = \lambda/\delta t$ with a relation to the kinematic viscosity by $\nu = \tau c_s^2 \delta t$. We now introduce a modified particle distribution function $\bar{f}_\alpha$ and its corresponding equilibrium distribution function $\bar{f}_\alpha^{eq}$ [32] defined as

$$\bar{f}_\alpha = f_\alpha + \frac{f_\alpha - f_\alpha^{eq}}{2\tau} - \frac{(\mathbf{e}_\alpha - \mathbf{u})\cdot \mathbf{G} f_\alpha^{eq}}{2\rho c_s^2}\delta t \tag{6}$$

and

$$\bar{f}_\alpha^{eq} = f_\alpha^{eq} - \frac{(\mathbf{e}_\alpha - \mathbf{u})\cdot \mathbf{G} f_\alpha^{eq}}{2\rho c_s^2}\delta t. \tag{7}$$

Substituting Eqs. (4)–(7) into Eq. (3), we have

$$\bar{f}_\alpha(\mathbf{x},t) = \bar{f}_\alpha(\mathbf{x}-\mathbf{e}_\alpha\delta t, t-\delta t) - \frac{1}{\tau+1/2}(\bar{f}_\alpha - \bar{f}_\alpha^{eq})\bigg|_{(\mathbf{x}-\mathbf{e}_\alpha\delta t, t-\delta t)} + \delta t \frac{(\mathbf{e}_\alpha - \mathbf{u})\cdot \mathbf{G} f_\alpha^{eq}}{\rho c_s^2}\bigg|_{(\mathbf{x}-\mathbf{e}_\alpha\delta t, t-\delta t)}. \tag{8}$$

Similar to the procedure in [31], we solve Eq. (8) in two steps:

- **Collision**

$$\bar{f}_\alpha^{*}(\mathbf{x}, t-\delta t) = \bar{f}_\alpha(\mathbf{x}, t-\delta t) - \frac{1}{\tau+1/2}(\bar{f}_\alpha - \bar{f}_\alpha^{eq})\bigg|_{(\mathbf{x}, t-\delta t)} + \delta t \frac{(\mathbf{e}_\alpha - \mathbf{u})\cdot \mathbf{G} f_\alpha^{eq}}{\rho c_s^2}\bigg|_{(\mathbf{x}, t-\delta t)}, \tag{9}$$

which is followed by the substitution $\bar{f}_\alpha(\mathbf{x}, t-\delta t) = \bar{f}_\alpha^{*}(\mathbf{x}, t-\delta t)$.

- **Streaming**

$$\bar{f}_\alpha(\mathbf{x},t) = \bar{f}_\alpha(\mathbf{x}-\mathbf{e}_\alpha\delta t, t-\delta t). \tag{10}$$

The density and momentum can be computed by taking moments as follows:

$$\rho = \sum_{\alpha=0}^{8} \bar{f}_\alpha \text{ and } \rho\mathbf{u} = \sum_{\alpha=0}^{8} \mathbf{e}_\alpha \bar{f}_\alpha + \frac{\delta t}{2}\mathbf{G}. \tag{11}$$

The streaming step can be expressed as a solution of the linear advection equation in an Eulerian framework [34], which can be written as follows:

$$\frac{\partial \bar{f}_\alpha}{\partial t} + \mathbf{e}_\alpha \cdot \nabla \bar{f}_\alpha = 0. \tag{12}$$

2.2. Energy equation: advection–diffusion equation

The temperature is modeled with the macroscopic energy equation. Assuming the flow to be incompressible and compression work due to pressure to be negligible, we can simplify the energy equation to the following advection–diffusion equation:

$$\frac{\partial T}{\partial t} + \mathbf{u}\cdot\nabla T = \chi \nabla^2 T, \tag{13}$$

where $\chi = \frac{\kappa}{\rho c_p}$ is the thermal diffusivity, c_p is the specific heat at constant pressure, and κ is the thermal conductivity.

3. Numerical discretization

In this section, we present our computational scheme. We provide details to the discontinuous Galerkin weak formulation, numerical fluxes, and boundary conditions for Eqs. (12) and (13). Details on the spectral element discretizations and time-stepping schemes are also discussed.

3.1. Weak formulation of the LB advection equation

We formulate a weak form of Eq. (12) defined on the computational domain $\Omega = \cup_{e=1}^{E} \Omega^e$ with nonoverlapping elements Ω^e. Choosing proper test functions ϕ_α, multiplying them with Eq. (12), and integrating by parts twice in a manner similar to [31], we obtain the following weak formulation:

$$\left(\frac{\partial \bar{f}_\alpha}{\partial t} + \nabla\cdot\mathbf{F}_\alpha(\bar{f}), \phi_\alpha\right)_{\Omega^e} = \left(\mathbf{n}\cdot\left[\mathbf{F}_\alpha(\bar{f}) - \mathbf{F}_\alpha^{*}(\bar{f})\right], \phi_\alpha\right)_{\partial\Omega^e}, \tag{14}$$

where $\mathbf{F}_\alpha(\bar{f}) = \mathbf{e}_\alpha \bar{f}_\alpha$ represents the flux vector with the microscopic velocities $\mathbf{e}_\alpha = (e_{\alpha x}, e_{\alpha y})$ and $\mathbf{n} = (n_x, n_y)$ is the unit normal vector pointing outward on the element boundary, $\partial\Omega^e$. The numerical flux $\mathbf{F}_\alpha^{*}(\bar{f}) = \mathbf{F}_\alpha^{*}(\bar{f}, \bar{f}^{+})$ in Eq. (14) is a function of the local solution $\bar{f}_\alpha$ and the neighboring solution $\bar{f}_\alpha^{+}$ at the interfaces between neighboring elements. We choose the Lax–Friedrichs flux in [31,35] expressed as the following:

$$\mathbf{n}\cdot(\mathbf{F}_\alpha - \mathbf{F}_\alpha^{*}) = \begin{cases} (\mathbf{n}\cdot\mathbf{e}_\alpha)[\bar{f}_\alpha - \bar{f}_\alpha^{+}] & \text{for } \mathbf{n}\cdot\mathbf{e}_\alpha < 0, \\ 0 & \text{for } \mathbf{n}\cdot\mathbf{e}_\alpha \geqslant 0. \end{cases} \tag{15}$$

When $\mathbf{n}\cdot\mathbf{e}_\alpha < 0$, we can write

$$\mathbf{n}\cdot(\mathbf{F}_\alpha - \mathbf{F}_\alpha^{*}) = (n_x e_{\alpha x} + n_y e_{\alpha y})\bar{f}_\alpha + (n_x^{+} e_{\alpha x} + n_y^{+} e_{\alpha y})\bar{f}_\alpha^{+}. \tag{16}$$

The proper upwinding scheme, inherent in the Lax-Friedrichs flux, allows momentum transfer at the element interface to depend only on those particles that are entering into the element.

Boundary conditions are weakly imposed through the numerical flux. The wall boundary condition, with specific details provided in [24,31], is given as follows:

$$\bar{f}_\alpha - \bar{f}_\alpha^{+} = \begin{cases} \bar{f}_\alpha - \bar{f}_{\alpha^*} - 2t_\alpha \rho_0 (\mathbf{e}_\alpha\cdot\mathbf{u}_b)/c_s^2 & \text{for } \mathbf{n}\cdot\mathbf{e}_\alpha < 0 \\ 0 & \text{for } \mathbf{n}\cdot\mathbf{e}_\alpha \geqslant 0, \end{cases} \tag{17}$$

where $\bar{f}_{\alpha^*}$ is the particle distribution function moving in the opposite direction of $\bar{f}_\alpha$, $\mathbf{u}_b$ is the macroscopic velocity prescribed at the wall boundary, and ρ_0 is the reference density, chosen to be unity.

3.2. Weak formulation of the advection–diffusion equation

Applying the incompressible assumption and expressing Eq. (13) as a system of first-order equations [35], we have

$$\frac{\partial T}{\partial t} + \nabla \cdot (\mathbf{u}T) = \nabla \cdot \mathbf{q}, \tag{18}$$

$$\mathbf{q} = \chi \nabla T. \tag{19}$$

We refer to $\mathbf{q}$ as the auxiliary variable. In addition, we define a flux vector by $\mathbf{F}(T) = \mathbf{u}T = (u_x T, u_y T)$ and introduce numerical fluxes $\mathbf{F}^*, \mathbf{q}^*$ and T^*. As was done for Eq. (14), we define proper test functions $\bar{\phi}$ and $\bar{\bar{\phi}}$ and obtain the following set of weak formulations for Eqs. (18) and (19) as

$$\left(\frac{\partial T}{\partial t} + \nabla \cdot (\mathbf{F}(T) - \mathbf{q}), \bar{\phi}\right)_{\Omega^e} = \left(\mathbf{n} \cdot [\mathbf{q}^* - \mathbf{q}] - \mathbf{n} \cdot [\mathbf{F}^* - \mathbf{F}], \bar{\phi}\right)_{\partial\Omega^e} \tag{20}$$

$$\left(\mathbf{q} - \chi \nabla T, \bar{\bar{\phi}}\right)_{\Omega^e} = \chi \left(\mathbf{n}[T^* - T], \bar{\bar{\phi}}\right)_{\partial\Omega^e}. \tag{21}$$

We use the Lax-Friedrich flux for $\mathbf{F}^*$ in Eq. (20), defined by

$$\mathbf{F}^*(T, T^+) = \frac{1}{2}[\mathbf{F}(T) + \mathbf{F}(T^+)] + \frac{C}{2}[\mathbf{n}(T - T^+)], \tag{22}$$

where

$$C = \max \left| \mathbf{n} \cdot \frac{\partial \mathbf{F}}{\partial T} \right| = \max |\mathbf{n} \cdot \mathbf{u}|, \tag{23}$$

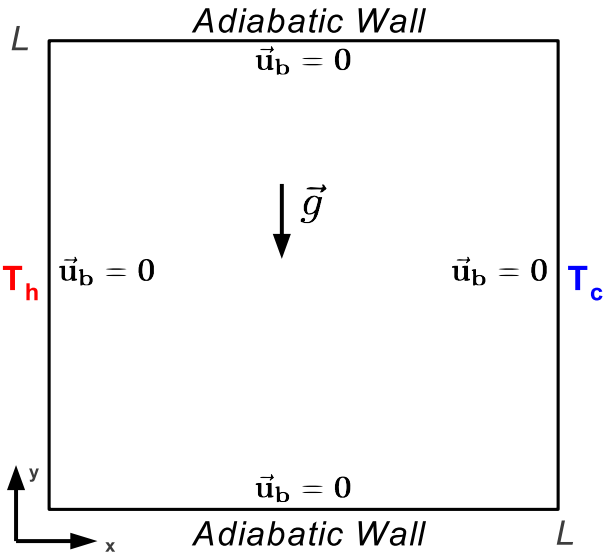

Fig. 2. Geometry and boundary conditions of natural convection in a square cavity.

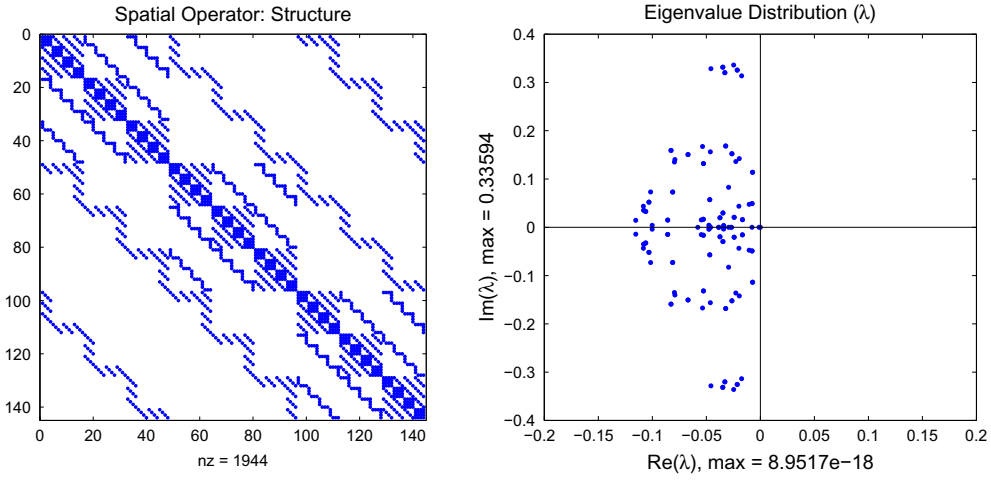

(a) Periodic Boundary Conditions

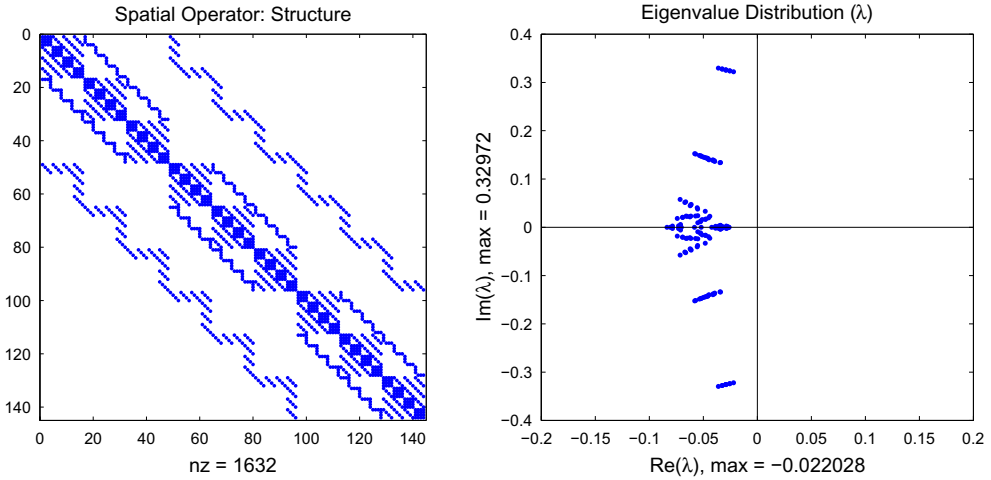

(b) Thermal Boundary Conditions

Fig. 1. Spatial operator (left) and eigenvalue spectrum (right) for Eq. (43) for $E = 9$ and $N = 3$ with periodic (a) and thermal (b) boundary conditions *nz* represents the number of non-zero elements in the spatial operator.

and the central flux for $\mathbf{q}^*$ and T^* in Eqs. (20) and (21), defined by

$$\mathbf{q}^* = \frac{1}{2}[\mathbf{q} + \mathbf{q}^+] \quad \text{and} \quad T^* = \frac{1}{2}[T + T^+]. \tag{24}$$

Boundary conditions are weakly imposed through the numerical flux [35]. For this paper, we are concerned with implementing two types of thermal wall boundary conditions: constant temperature (*i.e.* Dirichlet) and heat flux (*i.e.* Neumann) boundary conditions. Dirichlet boundary conditions are imposed through the primary variable, $T = T_w$, while Neumann boundary conditions are imposed via the auxiliary variable $\mathbf{q} = \mathbf{q}_w$. T_w and $\mathbf{q}_w$ represent the specified constant temperature and heat flux, respectively. We impose these conditions in the following way:

(i) Constant temperature (Dirichlet) boundary conditions, $T = T_w$

$$T^+ = -T + 2T_w, \ \mathbf{q}^+ = \mathbf{q}, \ (\mathbf{u}T)^+ = \mathbf{u}T. \tag{25}$$

(ii) Heat flux (Neumann) boundary conditions, $\mathbf{q} = \mathbf{q}_w$

$$T^+ = T, \ \mathbf{q}^+ = -\mathbf{q} + 2\mathbf{q}_w, \ (\mathbf{u}T)^+ = \mathbf{u}T. \tag{26}$$

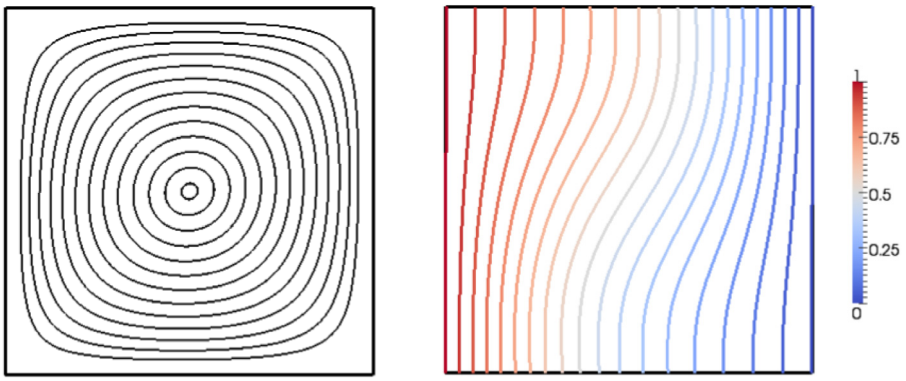

(a) $Ra = 10^3$, $Pr = 0.71$

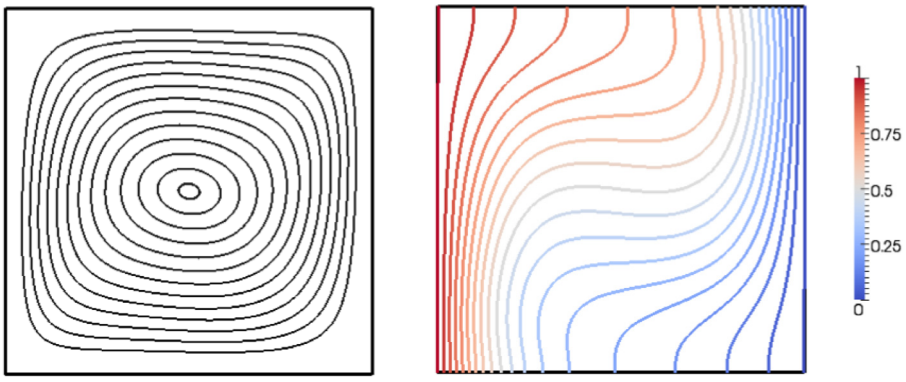

(b) $Ra = 10^4$, $Pr = 0.71$

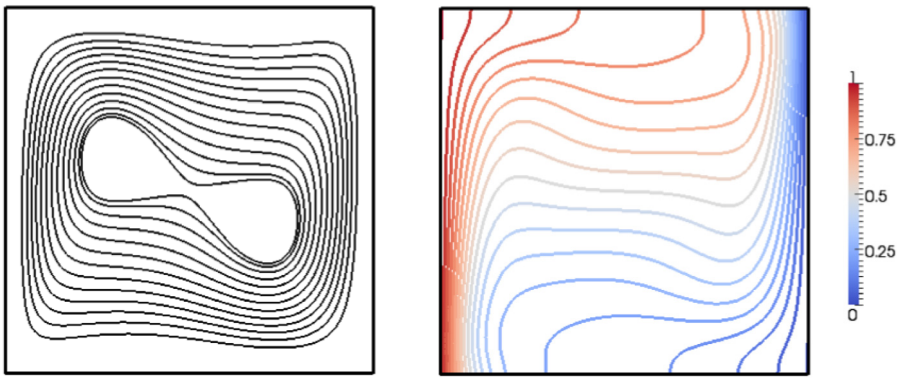

(c) $Ra = 10^5$, $Pr = 0.71$

Fig. 3. Streamlines (left) and isotherms (right) of natural convection cavity flow; $E = 256$ and $N = 5$.

3.3. Spectral element discretizations

We seek a local approximate solution u^N on Ω^e expressed by the finite expansion of the basis $\psi_{ij}(\xi,\eta)$ as

$$u^N(x,y,t) = \sum_{i,j=0}^{N} (u^N)_{ij}\psi_{ij}(\xi,\eta), \tag{27}$$

where $(u^N)_{ij} = u^N(x_i,y_j,t)$ represents the approximate solution u^N on the nodal points (x_i,y_j) at time t and $\psi_{ij}(\xi,\eta) = l_i(\xi(x))l_j(\eta(y))$, or simply ψ_{ij}, is the tensor product basis of the one-dimensional Legendre–Lagrange interpolation polynomials

$$l_i(\xi) = N(N+1)^{-1}(1-\xi^2)L'_N(\xi)/(\xi-\xi_i)L_N(\xi_i) \text{ for } \xi \in [-1,1], \tag{28}$$

based on the GLL quadrature nodes ξ_i where $L_N(\xi)$ is the Nth-order Legendre polynomial. The physcial domain $(x,y) \in \Omega^e$ is mapped to the reference domain $(\xi,\eta) \in [-1,1]^2$, through the Gordon-Hall mapping [36].

Let us denote our approximate solutions by $\bar{f}^N_\alpha$ for the density distribution functions, T^N for the temperature, and $q^N = (q^N_x, q^N_y)$ for the auxiliary function and express each component in the form

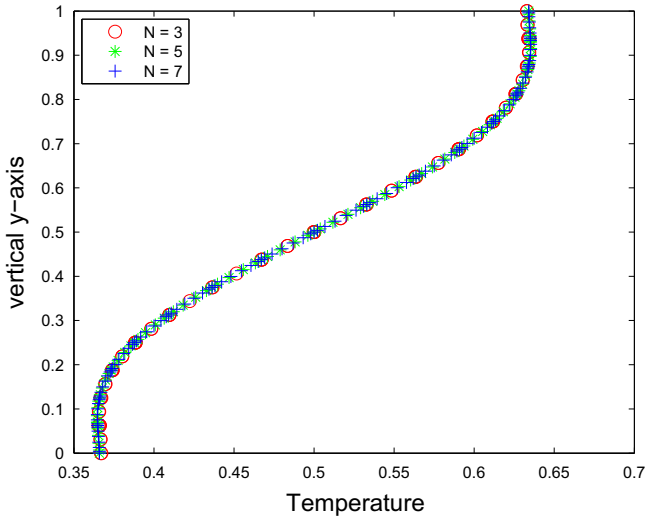

(a) Temperature Profile at $x = 0.5$

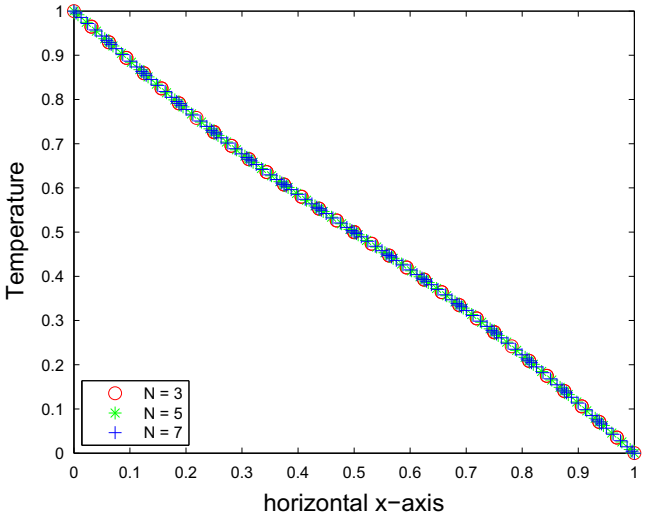

(b) Temperature Profile at $y = 0.5$

Fig. 4. Temperature profiles for natural convection square cavity flow at $Ra = 1000$, demonstrating convergence of the solution for increasing $N = 3, 5, 7$ with $E = 256$.

of (27). Choosing $\psi_{\bar{i}\bar{j}} = l_i(\xi(x))l_j(\eta(y))$ with a different index set for each test function $\phi_\alpha, \bar{\phi}$, and $\bar{\bar{\phi}}$ and plugging the approximate solutions into the corresponding weak formulations Eqs. (14), (20), and (21), we get a set of semidiscrete schemes

$$\frac{d\mathbf{f}_\alpha}{dt} + \mathbf{M}^{-1}\mathbf{D}_1\mathbf{f}_\alpha = \mathbf{M}^{-1}\mathbf{R}_1\mathbf{f}_\alpha, \tag{29}$$

$$\frac{d\mathbf{T}}{dt} + \mathbf{M}^{-1}\mathbf{D}_2\mathbf{T} - \mathbf{M}^{-1}\mathbf{D}\mathbf{q} = \mathbf{M}^{-1}(\mathbf{R}\mathbf{q} - \mathbf{R}_2\mathbf{T}), \tag{30}$$

$$\mathbf{q}_x - \chi\mathbf{M}^{-1}\mathbf{D}_x\mathbf{T} = \chi\mathbf{M}^{-1}\mathbf{R}_x\mathbf{T}, \tag{31}$$

$$\mathbf{q}_y - \chi\mathbf{M}^{-1}\mathbf{D}_y\mathbf{T} = \chi\mathbf{M}^{-1}\mathbf{R}_y\mathbf{T}, \tag{32}$$

where the solution vectors are defined by $\mathbf{f}_\alpha = [(\bar{f}^N_\alpha)_{ij}]$, $\mathbf{T} = [T^N_{ij}]$, and $\mathbf{q} = (\mathbf{q}_x, \mathbf{q}_y)$ with $\mathbf{q}_x = [(q^N_x)_{ij}]$ and $\mathbf{q}_y = [(q^N_y)_{ij}]$ on a local element. The mass matrix is defined as

$$\mathbf{M} = (\psi_{ij}, \psi_{\bar{i}\bar{j}})_{\Omega^e} = J(\hat{M} \otimes \hat{M}), \tag{33}$$

where $\hat{M}_{\bar{i}i} = \sum_{k=0}^{N} l_i(\xi_k)l_{\bar{i}}(\xi_k)w_k$ is the one-dimensional mass matrix with the quadrature weight w_k defined on the reference domain $[-1,1]$ and $J = [J_{ll}] = \text{diag}\{J_{ij}\}$ represents the value of the Jacobian at each node (x_i,y_j) with $l = i + (N+1)j$ on Ω^e. The one-dimensional mass matrix $\hat{M}$ is diagonal because of the orthogonal property of the Legendre-Lagrange interpolation polynomials on the GLL nodes, and thus the two-dimensional mass matrix $\mathbf{M}$ is also diagonal. The gradient matrices are defined by

$$\mathbf{D}_1 = e_{\alpha x}\mathbf{D}_x + e_{\alpha y}\mathbf{D}_y, \quad \mathbf{D}_2 = \mathbf{D}_x(u_x) + \mathbf{D}_y(u_y), \text{ and } \mathbf{D}\mathbf{q} = \mathbf{D}_x\mathbf{q}_x + \mathbf{D}_y\mathbf{q}_y, \tag{34}$$

Table 1
Convergence of Nu_o, Nu_o^{max}, and Nu_o^{min} for $Ra = 10^3$.

SEDG-LBM (N)	Nu_o	Nu_o^{max}	Nu_o^{min}
3	1.1165	1.5261	0.6847
5	1.1177	1.5063	0.6916
7	1.1178	1.5063	0.6913
9	1.1178	1.5063	0.6913
Wang et al. [39]	1.1178	1.5063	0.6912
De Vahl Davis [41]	1.117	1.505	0.692

Table 2
Convergence of Nu_o, Nu_o^{max}, and Nu_o^{min} for $Ra = 10^4$.

SEDG-LBM (N)	Nu_o	Nu_o^{max}	Nu_o^{min}
3	2.2236	3.7078	0.5413
5	2.2447	3.5303	0.5863
7	2.2448	3.5306	0.5852
9	2.2448	3.5309	0.5851
Wang et al. [39]	2.2448	3.5310	0.5849
Hortmann et al. [40]	2.24475	3.53087	–
De Vahl Davis [41]	2.238	3.528	0.586

Table 3
Convergence of Nu_o, Nu_o^{max}, and Nu_o^{min} for $Ra = 10^5$.

SEDG-LBM (N)	Nu_o	Nu_o^{max}	Nu_o^{min}
3	4.3187	9.5203	0.3362
5	4.5191	7.6878	0.7310
7	4.5216	7.7184	0.7295
9	4.5216	7.7189	0.7286
Wang et al. [39]	4.5214	7.7161	0.7279
Hortmann et al. [40]	4.52164	7.72013	–
De Vahl Davis [41]	4.509	7.717	0.729

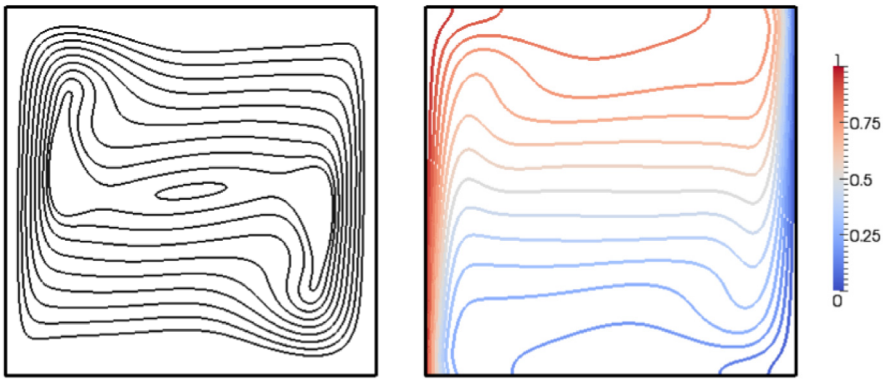

(a) $Ra = 10^6,\ Pr = 0.71$

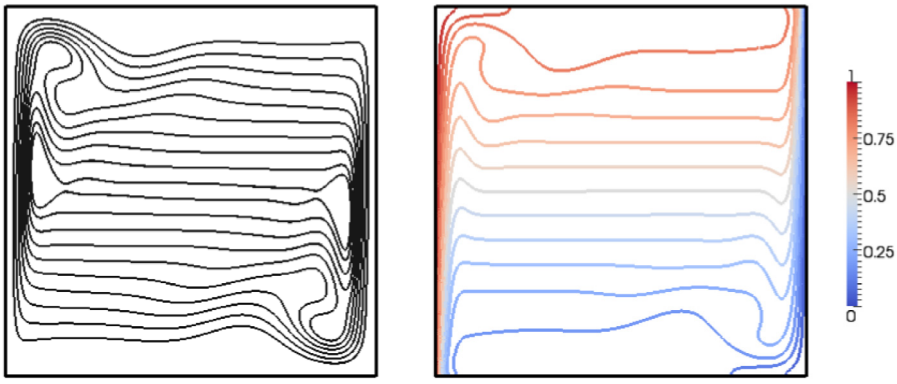

(b) $Ra = 10^7,\ Pr = 0.71$

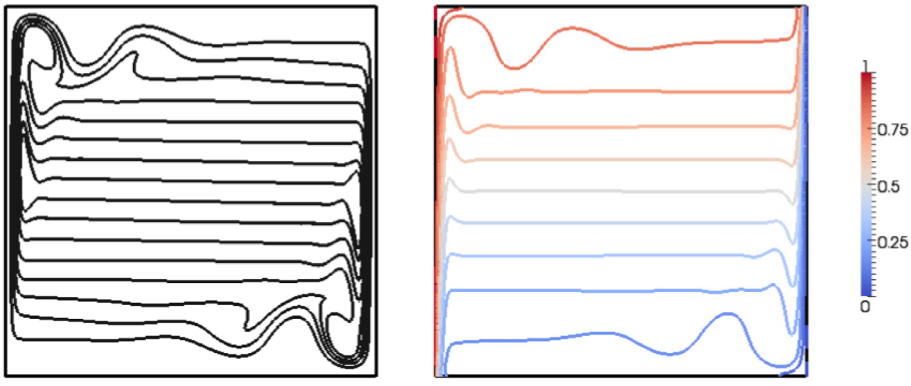

(c) $Ra = 10^8,\ Pr = 0.71$

Fig. 5. Streamlines (left) and isotherms (right) of natural convection cavity flow for $Ra > 10^5$.

where the differentiation matrices can be represented by a tensor product form of the one-dimensional differentiation matrix $\hat{D} = [\hat{D}_{ii}] = l_i'(\xi_i)$ as

$$\mathbf{D}_x = \left(\frac{\partial \psi_{ij}}{\partial x}, \psi_{\hat{i}\hat{j}}\right) = G^{\xi x} J[\hat{M} \otimes \hat{M}\hat{D}] + G^{\eta x} J[\hat{M}\hat{D} \otimes \hat{M}], \tag{35}$$

$$\mathbf{D}_y = \left(\frac{\partial \psi_{ij}}{\partial y}, \psi_{\hat{i}\hat{j}}\right) = G^{\xi y} J[\hat{M} \otimes \hat{M}\hat{D}] + G^{\eta y} J[\hat{M}\hat{D} \otimes \hat{M}], \tag{36}$$

Table 4
Computed Nusselt numbers, Nu_o, for $Ra = 10^6, 10^7, 10^8$.

Ra	10^6	10^7	10^8
SEDG-LBM	8.820	16.517	30.242
Wang et al. [39]	8.8192	–	–
Dixit and Babu [16]	8.805	16.79	30.506
Le Quéré [43]	8.8252	16.523	30.225

where $G^{\xi x}$, $G^{\xi y}$, $G^{\eta x}$, and $G^{\eta y}$ represent diagonal matrices for the geometric factors $\frac{\partial \xi}{\partial x}$, $\frac{\partial \xi}{\partial y}$, $\frac{\partial \eta}{\partial x}$, and $\frac{\partial \eta}{\partial x}$, respectively, at the nodal points (x_i, y_j). The surface integrations acting on the boundary nodes on each face of the local element in Eqs. (29)–(32) are represented by

$$\mathbf{R}_1\mathbf{f}_\alpha = \sum_{s=1}^{4}\sum_{k=0}^{N}\mathcal{R}_k^s\{\mathbf{n}\cdot[\mathbf{F}_\alpha(\bar{f}) - \mathbf{F}_\alpha^*(\bar{f})]\}w_k J_k^s, \tag{37}$$

$$\mathbf{R}_2\mathbf{T} = \sum_{s=1}^{4}\sum_{k=0}^{N}\mathcal{R}_k^s\left\{\mathbf{n}\cdot[\mathbf{F}^*(T)_{ij} - \mathbf{F}(T)_{ij}]\right\}w_k J_k^s, \tag{38}$$

$$\mathbf{R}\mathbf{q} = \sum_{s=1}^{4}\sum_{k=0}^{N}\mathcal{R}_k^s\left\{\mathbf{n}\cdot[\mathbf{q}_{ij}^* - \mathbf{q}_{ij}]\right\}w_k J_k^s, \tag{39}$$

$$\mathbf{R}_x\mathbf{T} = \sum_{s=1}^{4}\sum_{k=0}^{N}\mathcal{R}_k^s\{n_x[(T)_{ij}^* - (T)_{ij}]\}w_k J_k^s, \tag{40}$$

$$\mathbf{R}_y\mathbf{T} = \sum_{s=1}^{4}\sum_{k=0}^{N}\mathcal{R}_k^s\{n_y[(T)_{ij}^* - (T)_{ij}]\}w_k J_k^s, \tag{41}$$

where $R_k^s\{\cdot\}$ extracts the information of $\{\cdot\}$ at the nodes situated on each face of the local element for the face number s and J_k^s is the surface Jacobian at the nodes on each face.

The semidiscrete schemes for Eqs. (29) and (30) can be written simply as

$$\frac{d\mathbf{f}_\alpha}{dt} = \mathbf{L}_1\mathbf{f}_\alpha, \tag{42}$$

$$\frac{d\mathbf{T}}{dt} = \mathbf{L}_2\mathbf{T} + \mathbf{M}^{-1}\mathbf{D}\mathbf{q} + \mathbf{M}^{-1}\mathbf{R}\mathbf{q}, \tag{43}$$

where $\mathbf{L}_1 = \mathbf{M}^{-1}(-\mathbf{D}_1 + \mathbf{R}_1)$ and $\mathbf{L}_2 = \mathbf{M}^{-1}(-\mathbf{D}_2 - \mathbf{R}_2)$. We have shown the eigenvalue distributions for the spatial operator of Eq. (42) in [31]. Fig. 1 shows the matrix structure and eigenvalue (λ) distribution for the spatial operator in Eq. (43) with periodic (Fig. 1(a)) and non-periodic (Fig. 1(b)) boundary conditions. The non-periodic boundary conditions include the thermal (i.e. Dirichlet and Neumann) boundary formulations, which were written in Eqs. (25) and (26). A uniform spectral element mesh is used with the number of elements $E = 3\times 3$ and polynomial order $N = 3$. For convenience, we set the velocity $\mathbf{u} = (1,1)$ and $\chi = 1$. Eigenvalues with positive real parts, Re (λ), can lead to numerical solutions which grow dramatically in time and lead to instability. Fig. 1 shows that the eigenvalue distributions reside entirely in the negative half-plane. As a result, we can choose the fourth-order, five-stage low-storage Runge–Kutta (RK) time integration method [37] which has a slightly larger stability region and requires less memory than the classical RK methods.

4. Computational results

In this section, we show computational results and validation for two benchmark problems: natural convection in a square cavity and a horizontal concentric annulus in two dimensions. We begin with a brief discussion of how relevant parameters are determined.

4.1. Parameters for benchmark studies

For natural convection flows, we consider a Bousinessq approximation [9] for the force term $\mathbf{G}$ in Eqs. (1) and (11) defined as

$$\mathbf{G} = \rho\mathbf{g}\beta(T - T_o), \tag{44}$$

where $T_o = (T_h + T_c)/2$ is the average of two different characteristic temperatures in our benchmark problems ($T_h > T_c$), $\mathbf{g}$ is the gravitational acceleration, and β is the thermal expansion coefficient. In accordance with the Bousinessq approximation, β is constant in space and time.

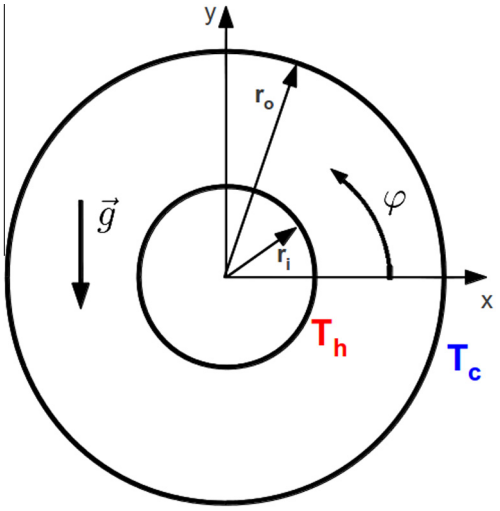

Fig. 6. Geometry and boundary conditions of natural convection in a horizontal concentric annulus.

We characterize natural convection flows with two nondimensional numbers, the Rayleigh number (Ra) and the Prandtl number (Pr). They are defined as follows:

$$Ra = \frac{\beta|\mathbf{g}|(T_h - T_c)L^3}{\nu\chi} \text{ and } Pr = \frac{\nu}{\chi}, \tag{45}$$

where L is a characteristic length of the computational domain, χ is the thermal diffusivity, and ν is the kinematic viscosity. We define the characteristic velocity as

$$U^* = \sqrt{\frac{Ra}{Pr}}\frac{\nu}{L}. \tag{46}$$

We ensure that our characteristic velocity is in the low Mach number regime, typically $Ma = 0.01$, so that

$$U^* \leqslant c_s Ma. \tag{47}$$

The dimensionless relaxation time τ is determined through the relation $\nu = \tau c_s^2\delta t$ where we determine the time-step size δt from $CFL = \frac{\max_\alpha|\mathbf{e}_\alpha|\delta t}{\Delta\mathbf{x}_{\min}} = 0.1$. $\Delta\mathbf{x}_{\min}$ is the minimum grid spacing in our mesh.

4.2. Natural convection in a square cavity

We performed steady-state natural convection flow simulations in a square cavity. The geometry is shown in Fig. 2. The initial velocity is set as $\mathbf{u} \equiv (0,0)$ and the initial density as $\rho \equiv 1$. The wall boundary conditions for the velocity fields are given as $\mathbf{u}_b = (0,0)$ and the nonhomogeneous Dirichlet boundary conditions for the temperature as $T(0,y,t) = T_h$ and $T(L,y,t) = T_c$. The adiabatic boundary conditions are set as $\frac{\partial T}{\partial y}|_{(x,0,t)} = \frac{\partial T}{\partial y}|_{(x,L,t)} = 0$.

Fig. 3 shows the streamlines and isotherms of the square cavity flows at $Ra = 10^3, 10^4$ and 10^5. The effect of Ra is evident in these figures. In particular, a given isotherm is passively advected throughout the domain to a greater degree as Ra increases. Results for $Ra \leqslant 10^5$ are performed on a uniform spectral element mesh with $E = 256$ and a fixed polynomial order of $N = 5$. The total number of grid points are given by $\mathcal{N} = (N+1)^2E$. Fig. 4 demonstrates good convergence of the temperature profiles with increasing polynomial order N on the same mesh. The profiles are shown at the vertical line $x = 0.5$ (Fig. 4(a)) and at the horizontal line $y = 0.5$ (Fig. 4(b)).

We also show the convergence of the Nusselt number, Nu_o, along the axis $x = 0$, where the Dirichlet boundary condition $T = T_h$ is specified. The Nusselt number is defined as

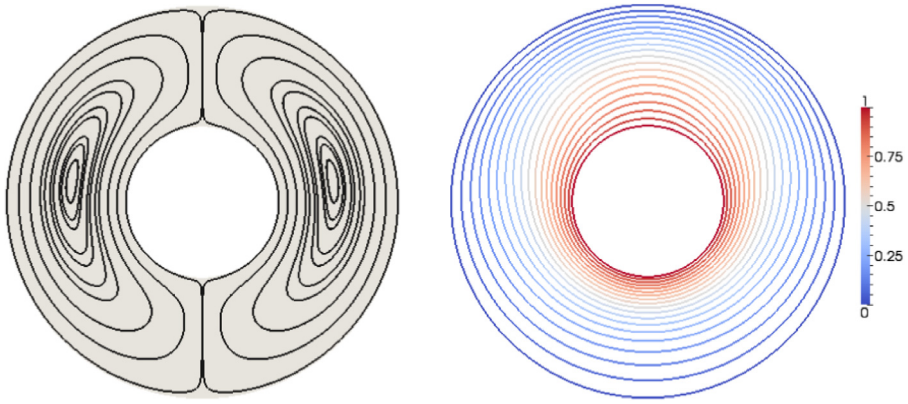

(a) $Ra = 10^3,\ Pr = 0.7$

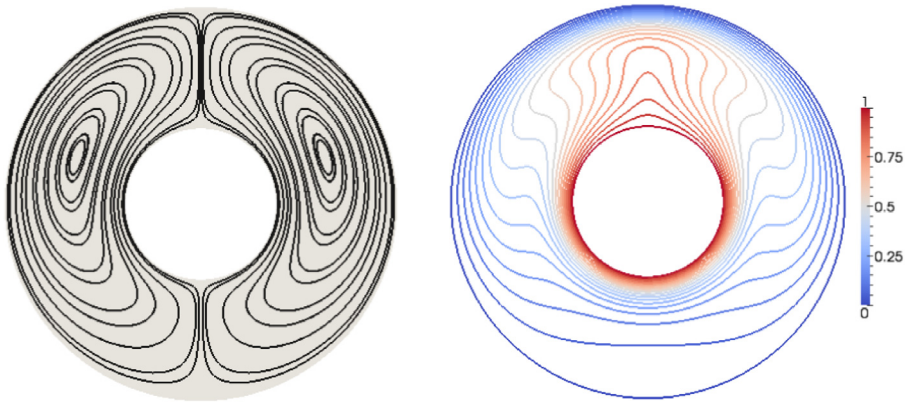

(b) $Ra = 10^4,\ Pr = 0.7$

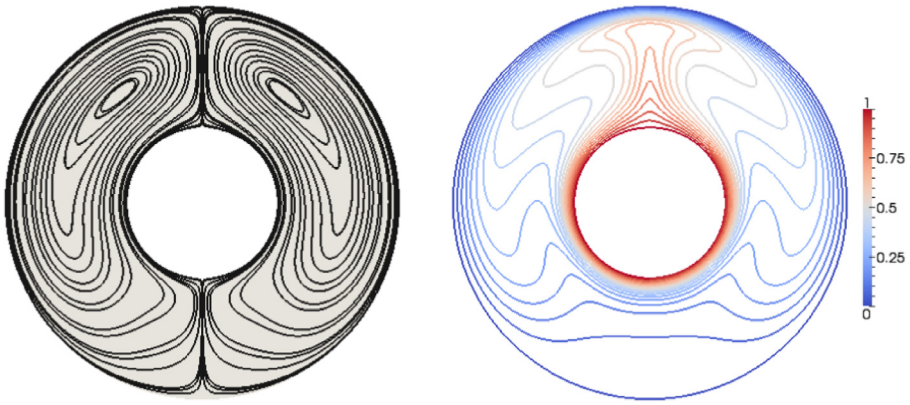

(c) $Ra = 5 \times 10^4,\ Pr = 0.7$

Fig. 7. Streamlines (left) and isotherms (right) of natural convection in a horizontal annulus, using $N = 5$ on Mesh *A*.

$$Nu_o = \int_0^1 q_x|_{x=0} dy, \tag{48}$$

where

$$q_x = u_x T - \frac{\partial T}{\partial x}. \tag{49}$$

In Tables 1–3, we present convergence studies of the Nusselt number for varying polynomial order $N = 3, 5, 7, 9$, including local minimum and maximum values. Validation is conducted by comparing Nusselt numbers to the work of Wang et al. [39], Hortmann et al. [40] and De Vahl Davis [41]. Our results are in good agreement with their results.

We take advantage of our high-order discretization and present results for Rayleigh numbers $Ra > 10^5$. Fig. 5 shows the streamlines and isotherms in the square cavity for $Ra = 10^6, 10^7$, and 10^8. For $Ra = 10^6$ and 10^7, the resolution of these simulations are performed on a uniform spectral element mesh with $E = 576$ and a fixed polynomial of order $N = 9$. And to capture even larger gradients near the walls, a uniform resolution of $E = 1024$ with $N = 9$ was used for $Ra = 10^8$.

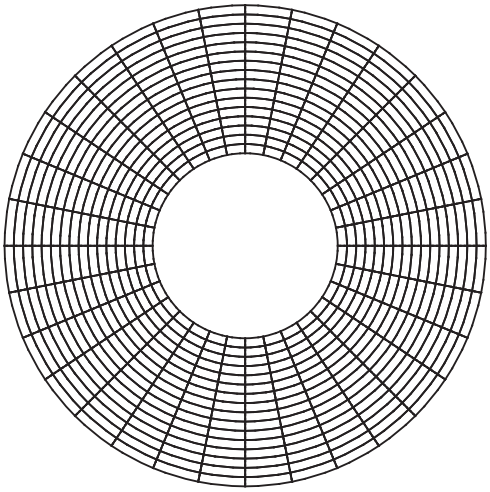

(a) Mesh A with $E = 512$

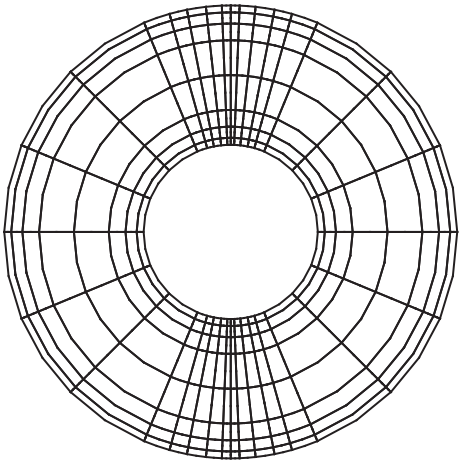

(b) Mesh B with $E = 256$

Fig. 8. Two different meshes used for the horizontal annulus simulations.

The effect of convection dominated heat transfer is evident in these figures and in the calculation of the Nusselt number, Nu_o, which can be seen in Table 4. As the Rayleigh number is increased, we can see that the flow toward the center of the square becomes parallel to the adiabatic (horizontal) boundaries. This is evident in the streamlines. The parallel flow phenomenon was also reported in the simulations of Dixit and Babu [16]. We also observe a more stratified flow where cooler fluid remains on the bottom of the cavity while hotter fluid resides on the top–as should be expected in natural convection. And with larger Rayleigh number, we notice the thinning of the boundary layer which results in the steeper temperature gradients. The effect of the larger Rayleigh number can be seen in Table 4, which shows that the computed Nusselt number (i.e. a nondimensional temperature gradient) agrees well with the results in the literature.

4.3. Natural convection in a horizontal concentric annulus

We studied steady-state natural convection flows inside a horizontal concentric annulus. The geometry and boundary conditions of the problem are provided in Fig. 6.

We set the initial velocity $\mathbf{u} \equiv (\mathbf{0}, \mathbf{0})$ and the initial density $\rho \equiv 1$. Wall boundary conditions for the velocity field are $\mathbf{u}_b = (0, 0)$, and temperature boundary conditions are given as $T(r = r_i, \varphi, t) = T_h = 1$ and $T(r = r_o, \varphi, t) = T_c = 0$. We use the radius ratio $\frac{r_o}{r_i} = 2.6$ and the characteristic length $L = r_o - r_i$.

Fig. 7 shows the streamlines and isotherms of the horizontal annulus cavity flows at $Ra = 10^3, 10^4, 5 \times 10^4$ on a spectral element mesh (see Fig. 8(a)) with $E = 512$ and $N = 5$. Again, the effect of Ra is evident. For $Ra = 10^3$, we can observe how diffusion dominates the hydrodynamic and temperature behavior. In this case, the isotherms are nearly circular with slight eccentricity near the top of the inner cylinder. The streamlines indicate how the flow is nearly symmetric about the horizontal ($\varphi = 0$) with the innermost streamline (central vortex) maintaining its position near $\varphi = 0$. We take note that vertical symmetry, about $\varphi = \frac{\pi}{2}$ and $\varphi = -\frac{\pi}{2}$, persists due to the concentric geometry of the domain. As Ra increases, we see how the isotherms deviate from the circular pattern and the effect of convection results in a "plume-like" pattern near $\varphi = \frac{\pi}{2}$. The innermost streamline (central vortex) also feels the effect of the Ra and we observe that there is a "migration" of this streamline towards $\varphi = \frac{\pi}{2}$. Temperature gradients near the boundaries seem to be increasing with Ra and we study this effect by computing average Nusselt numbers. The average Nusselt number Nu_{avg} is defined by

$$Nu_{avg} = \frac{1}{2}(Nu_{inner} + Nu_{outer}), \tag{50}$$

where

$$Nu_{inner} = -\frac{1}{\pi}\int_{-\frac{\pi}{2}}^{\frac{\pi}{2}} r_i \frac{\partial T}{\partial r}\Big|_{r=r_i} d\varphi, \tag{51}$$

$$Nu_{outer} = -\frac{1}{\pi}\int_{-\frac{\pi}{2}}^{\frac{\pi}{2}} r_o \frac{\partial T}{\partial r}\Big|_{r=r_o} d\varphi. \tag{52}$$

Tables 5–7 show convergence of the average Nusselt number Nu_{avg} on Mesh A with increasing polynomial order $N = 3, 5, 7, 9$. We com-

Table 5
Convergence of Nu_{avg} for $Ra = 10^3$.

SEDG-LBM (N) on Mesh A	Nu_{avg}
3	1.1295
5	1.1325
7	1.1325
9	1.1325
Kuehn and Goldstein [42]	1.083

Table 6
Convergence of Nu_{avg} for $Ra = 10^4$.

SEDG-LBM (N) on Mesh A	Nu_{avg}
3	2.0615
5	2.0704
7	2.0705
9	2.0705
Kuehn and Goldstein [42]	2.008

Table 7
Convergence of Nu_{avg} for $Ra = 5 \times 10^4$.

SEDG-LBM (N) on Mesh A	Nu_{avg}
3	3.0309
5	3.0950
7	3.0956
9	3.0956
Kuehn and Goldstein [42]	2.999

pare our results with those by Kuehn and Goldstein [42], who solve the Navier–Stokes equations by a finite-difference method. When compared with the results by Kuehn and Goldstein, our results are within 5% accuracy.

We examined details of the difference between our SEDG-LBM results and those from [42] in the temperature profiles at $\varphi = -\frac{\pi}{2}, 0, \frac{\pi}{2}$, demonstrating the comparison in Fig. 9. We observe that the SEDG-LBM results agree well with those by Kuehn and Goldstein for $\varphi = 0$. However, we observe some discrepancy in the range of $r^* = 0.1 \sim 0.3$ and $r^* = 0.2 \sim 0.9$ for the cases of $\varphi = -\frac{\pi}{2}$ and $\varphi = \frac{\pi}{2}$, respectively, as shown in Fig. 9. This difference might be due to the low resolution used in [42], which would explain the discrepancy in the comparison of Nu_{avg} in Tables 5–7.

Given this difference in Nu_{avg} and temperature profile, we further seek to verify our results against another benchmark. For this study, we simulate natural convection within a horizontal concentric annulus using Nek5000 [38], an open-source Navier–Stokes solver based on the spectral-element method. Using Nek5000 on Mesh A with a high polynomial approximation, $N = 11$, we determine temperature profiles and average Nusselt numbers and use this data as new benchmarks. Our SEDG-LBM simulations are performed on Mesh B (see Fig. 8(b)) with $E = 256$. Fig. 10 demonstrates the convergence of temperature profiles for our SEDG-LBM results at $\varphi = -\frac{\pi}{2}, 0, \frac{\pi}{2}$ for $Ra = 5 \times 10^4$ and $Pr = 0.7$. The results show good agreement with the Nek5000 solver.

In Tables 8–10, we show the convergence of Nu_{avg} with $N = 3, 5, 7, 9$ by the SEDG-LBM on Mesh B for $Ra = 10^3, 10^4$ and 5×10^4. Our results agree well with those determined by Nek5000. These tables show the advantage of the SEDG approximation. In particular, on the non-uniform coarse mesh (i.e. Mesh B) which exhibits biased resolution in the boundary layer region, SEDG-LBM results achieve the same accuracy as the SEDG-LBM results determined on the refined mesh (i.e. Mesh A) as given in Tables 5–7.

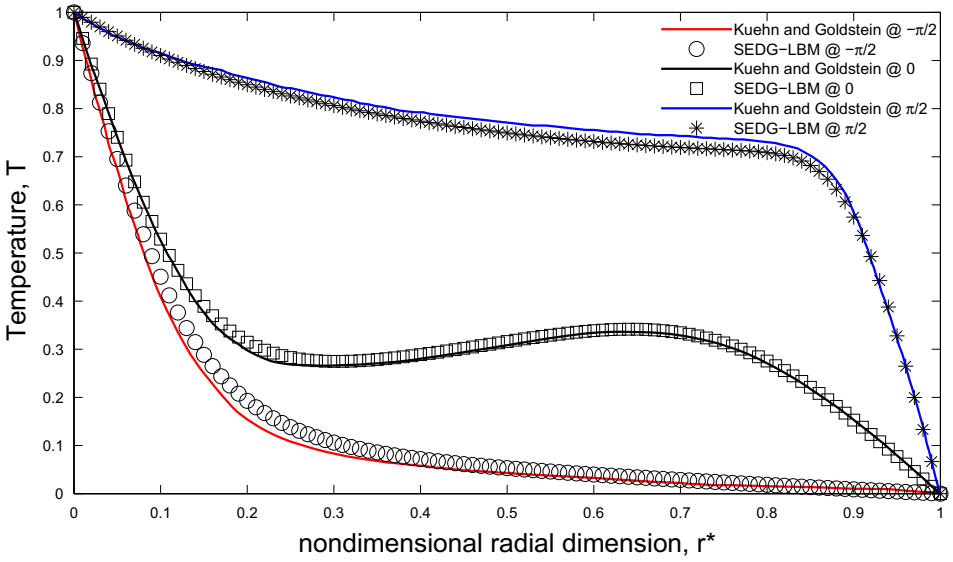

Fig. 9. Temperature profiles of SEDG-LBM results vs. those in Ref. [42] for horizontal annulus simulation at $Ra = 5 \times 10^4$ and $Pr = 0.7$ for $\varphi = \frac{\pi}{2}, \varphi = 0$, and $\varphi = -\frac{\pi}{2}$. Polynomial order for SEDG-LBM is $N = 9$. The nondimensional radius, r^* is defined as $r^* = \frac{r - r_i}{L}$. SEDG-LBM computations were performed on Mesh A.

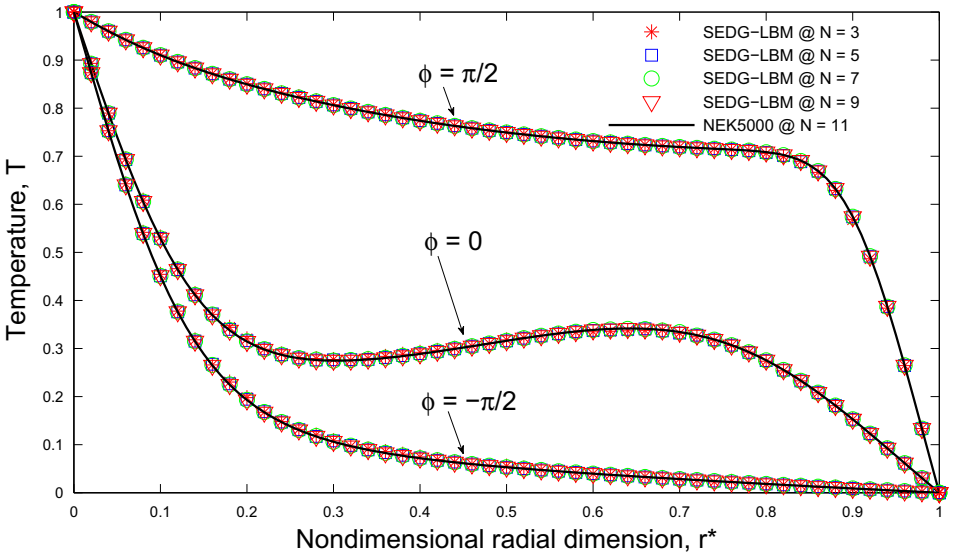

Fig. 10. Temperature profile of SEDG-LBM results vs. Nek5000 [38] for horizontal annulus simulation at $Ra = 5 \times 10^4$ and $Pr = 0.7$ for $\varphi = \frac{\pi}{2}, \varphi = 0$, and $\varphi = -\frac{\pi}{2}$. Polynomial orders for SEDG-LBM are $N = 3, 5, 7$ and 9. Polynomial order for Nek5000 is $N = 11$. SEDG-LBM computations were performed on Mesh B. Nek5000 computations were performed on Mesh A.

Table 8
Convergence of Nu_{avg} for $Ra = 10^3$.

SEDG-LBM (N) on Mesh B	Nu_{avg}
3	1.2034
5	1.1310
7	1.1325
9	1.1325
Nek5000 ($N = 11$)	1.1325

Table 9
Convergence of Nu_{avg} for $Ra = 10^4$.

SEDG-LBM (N) on Mesh B	Nu_{avg}
3	2.2195
5	2.0774
7	2.0702
9	2.0705
Nek5000 ($N = 11$)	2.0705

Table 10
Convergence of Nu_{avg} for $Ra = 5 \times 10^4$.

SEDG-LBM (N) on Mesh B	Nu_{avg}
3	3.0218
5	3.1055
7	3.0975
9	3.0958
Nek5000 ($N = 11$)	3.0956

5. Conclusions

We have presented a spectral-element discontinuous Galerkin lattice Boltzmann method for solving two-dimensional incompressible natural convection flows. In particular, we have presented results for natural convection in a square cavity and a horizontal concentric annulus. Our formulation extends the work of Min and Lee [31] by including a forcing term, defined by the Bousinessq approximation, in the discrete Boltzmann and lattice Boltzmann equations. We resolved the temperature field by applying an SEDG discretization in space to the advection–diffusion equation. In addition, boundary conditions were weakly imposed through a proper treatment of the numerical flux based on the Lax-Friedrichs and central fluxes. We used a passive-scalar approach that allows us to investigate flows for variable Prandtl number and to compute the temperature field cost-effectively by solving only one equation, rather than solving multiple equations as in the double-distribution approach. We have examined square cavity flows for $Ra = 10^3$–10^8 and flows in a horizontal concentric annulus for $Ra = 10^3$–5×10^4. Polynomial convergence studies for temperature profiles and Nusselt numbers have also been conducted. Computational results show good agreement with those results computed by a finite-difference method, a finite-volume method, a multiple-relaxation-time LBM, and a spectral element method [38].

Future work includes extension to three dimensions and performance studies in comparison with other approaches, such as double-distribution thermal lattice Boltzmann methods.

Acknowledgments

This work is supported in part by the U.S. Department of Energy, Office of Nuclear Energy's Nuclear Energy University Programs, and in part by the U.S. Department of Energy, under Contract DE-ACO2-O6CH11357. We thank Alexsandr Obabko for his help and guidance in the proper execution of the Nek5000 code.

References

[1] Alexander FJ, Chen S, Sterling JD. Lattice Boltzmann thermohydrodynamics. Phys Rev E 1993;47(4):R2249.
[2] Chen Y, Ohashi H, Akiyama M. Thermal lattice Bhatnagar–Gross–Krook model without nonlinear deviations in macrodynamic equations. Phys Rev E 1994;50(4):2776–83.
[3] Shan X, Chen H. Lattice Boltzmann model for simulating flows with multiple phases and components. Phys Rev E 1993;47(3):1815–9.
[4] McNamara GR, Garcia AL, Alder BJ. Stabilization of thermal lattice Boltzmann models. J Stat Phys 1995;81:395–408. 1/2.
[5] Vahala G, Pavlo P, Vahala L, Martys NS. Thermal lattice-Boltzmann models (TLBM) for compressible flows. Int J Mod Phys C 1998;9(8):1247–61.
[6] Prasianakis NI, Karlin IV. Lattice Boltzmann method for thermal flow simulation on standard lattices. Phys Rev E 2007;76:016702.
[7] Watari M, Tsutahara M. Two-dimensional thermal model of the finite-difference lattice Boltzmann method with high spatial isotropy. Phys Rev E 2003;67:036306.
[8] Soe M, Vahala G, Pavlo P, Vahala L, Chen H. Thermal lattice Boltzmann simulations of variable Prandtl number turbulent flows. Phys Rev E 1998;57(4):4227–37.
[9] Shan X. Simulation of Rayleigh–Bénard convection using a lattice Boltzmann method. Phys Rev E 1997;55(3):2780–8.
[10] He X, Chen S, Doolen GD. A novel thermal model for the lattice Boltzmann method in incompressible limit. J Comput Phys 1998;146(1):282–300.
[11] Palmer B, Rector D. Lattice Boltzmann algorithm for simulating thermal flow in compressible fluids. J Comput Phys 2000;161(1):1–20.
[12] Peng Y, Shu C, Chew YT. Simplified thermal lattice Boltzmann model for incompressible thermal flows. Phys Rev E 2003;68:026701.
[13] Shi Y, Zhao TS, Guo ZL. Thermal lattice Bhatnagar–Gross–Krook model for flows with viscous heat dissipation in the incompressible limit. Phys Rev E 2004;70:066310.
[14] Guo Z, Zheng C, Shi B, Zhao TS. Thermal lattice Boltzmann equation for low Mach number flows: decoupling model. Phys Rev E 2007;75:036704.
[15] Nor Azwadi CS, Tanahashi T. Simplified thermal lattice Boltzmann in incompressible limit. Int J Mod Phys B 2006;20(17):2437–49.
[16] Dixit HN, Babu V. Simulation of high Rayleigh number natural convection in a square cavity using the lattice Boltzmann method. Int J Heat Mass Trans 2006;49(3):727–39.
[17] He X, Luo LS, Dembo M. Some progress in lattice Boltzmann method. Part 1. Nonuniform mesh grids. J Comput Phys 1996;129:357–63.
[18] Shi Y, Zhao TS, Guo ZL. Finite difference-based lattice Boltzmann simulation of natural convection heat transfer in a horizontal concentric annulus. Comput Fluids 2006;35(1):1–15.
[19] Guo Z, Zhao TS. Explicit finite-difference lattice Boltzmann method for curvilinear coordinates. Phys Rev E 2003;67:066709.
[20] Shu C, Peng Y, Chew YT. Simulation of natural convection in a square cavity by Taylor series expansion- and least squares-based lattice Boltzmann method. Int J Mod Phys C 2002;13(10):1399–414.
[21] Peng Y, Chew YT, Shu C. Numerical simulation of natural convection in a concentric annulus between a square outer cylinder and a circular inner cylinder using the Taylor-series-expansion and least-squares-based lattice Boltzmann method. Phys Rev E 2003;67:026701.
[22] Succi S, Amati G, Benzi R. Challenges in lattice Boltzmann computing. J Stat Phys 1995;81:5–16.
[23] Lallemand P, Luo L-S. Theory of the lattice Boltzmann method: Acoustic and thermal properties in two and three dimensions. Phys Rev E 2003;68:036706.
[24] Zou Q, He X. On pressure and velocity boundary conditions for the lattice Boltzmann BGK model. Phys Fluids 1997;9(6):1591–8.
[25] Filippova O, Hänel D. Grid refinement for lattice-BGK models. J Comput Phys 1998;147(1):219–28.
[26] Mei R, Luo L-S, Shyy W. An accurate curved boundary treatment in the lattice Boltzmann method. J Comput Phys 1999;229(2):307–30.
[27] Lallemand P, Luo L-S. Lattice Boltzmann method for moving boundaries. J Comput Phys 2003;184(2):406–21.
[28] D'Orazio A, Corcione M, Celata GP. Application to natural convection enclosed flows of a lattice Boltzmann BGK model coupled with a general purpose thermal boundary condition. Int J Heat Mass Trans 2004;436:575–86.
[29] Tang GH, Tao WQ, He YL. Thermal boundary condition for the thermal lattice Boltzmann equation. Phys Rev E 2005;72:016703.
[30] Liu C-H, Lin K-H, Mai H-C, Lin C-A. Thermal boundary conditions for thermal lattice Boltzmann simulations. Comput Math Appl 2010;59(7):2178–93.
[31] Min M, Lee T. A spectral-element discontinuous Galerkin lattice Boltzmann method for nearly incompressible flows. J Comput Phys 2011;230(1):245–59.
[32] He X, Shan X, Doolen GD. Discrete Boltzmann equation model for nonideal gases. Phys Rev E 1998;57(1):R13.
[33] Qian YH, D'Humières D, Lallemand P. Lattice BGK models for Navier–Stokes equation. Europhys Lett 1992;17:479–84.
[34] Lee T, Lin C-L. An Eulerian description of the streaming process in the lattice Boltzmann equation. J Comput Phys 2003;185(2):445–71.

[35] Hesthaven JS, Warburton T. Nodal discontinuous Galerkin methods, algorithms, analysis, and applications. In: Texts in applied mathematics. Springer; 2008.
[36] Deville MO, Fischer PF, Mund EH. High-order methods for incompressible fluid flow. In: Cambridge monographs on applied and computational mathematics. Cambridge University Press; 2002.
[37] M.H. Carpenter, C. Kennedy, Fourth-order 2N-storage Runge–Kutta schemes, NASA Report TM 109112, NASA Langley Research Center; 1994..
[38] Fischer P, Lottes J, Pointer D, Siegel A. Petascale algorithms for reactor hydrodynamics. J Phys: Conf Ser 2008;125(1):012076.
[39] Wang J, Wang D, Lallemand P, Luo L. Lattice Boltzmann simulations of thermal convective flows in two dimensions. Comp Math Appl 2013;65(2):262–86.
[40] Hortmann M, Perić M, Scheuerer G. Finite volume multigrid prediction of laminar natural convection: Bench-mark solutions. Int J Numer Meth Fluids 1990;11(2):189–207.
[41] De Vahl Davis G. Natural convection of air in a square cavity: a benchmark numerical solution. Int J Numer Meth Fluids 1983;3(3): 249–64.
[42] Kuehn TH, Goldstein RJ. An experimental and theoretical study of natural convection in the annulus between horizontal concentric cylinders. J Fluid Mech 1976;74(4):695–719.
[43] Le Quéré P. Accurate solutions to the square thermally driven cavity at high Rayleigh number. Comp Fluids 1991;20(1):29–41.